

# Operando Spectroscopic Analysis of an Amorphous Cobalt Sulfide Hydrogen Evolution Electrocatalyst

Nikolay Kornienko,<sup>†</sup> Joaquin Resasco,<sup>‡</sup> Nigel Becknell,<sup>†</sup> Chang-Ming Jiang,<sup>†</sup> Yi-Sheng Liu,<sup>§</sup> Kaiqi Nie,<sup>§,||</sup> Xuhui Sun,<sup>||</sup> Jinghua Guo,<sup>§</sup> Stephen R. Leone,<sup>†,⊥,#</sup> and Peidong Yang<sup>\*,†,∇,○</sup>

<sup>†</sup>Department of Chemistry, University of California, Berkeley, Berkeley, California 94720, United States

<sup>‡</sup>Department of Chemical Engineering, University of California, Berkeley, Berkeley, California 94720, United States

<sup>§</sup>Advanced Light Source, Lawrence Berkeley National Laboratory, Berkeley, California 94720, United States

<sup>||</sup>Soochow University-Western University Centre for Synchrotron Radiation Research, Institute of Functional Nano and Soft Materials (FUNSOM) and Collaborative Innovation Center of Suzhou Nano Science & Technology, Soochow University, Suzhou 215123, China

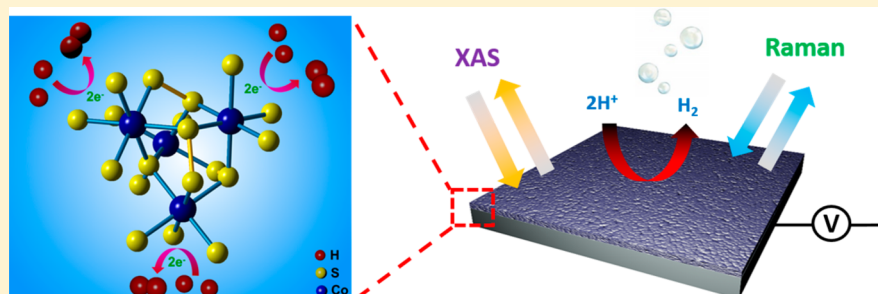
<sup>⊥</sup>Chemical Sciences Division, Lawrence Berkeley National Laboratory, 1 Cyclotron Road, Berkeley, California 94720, United States

<sup>#</sup>Department of Physics, University of California, Berkeley, Berkeley, California 94720, United States

<sup>∇</sup>Materials Sciences Division, Lawrence Berkeley National Laboratory, 1 Cyclotron Road, Berkeley, California 94720, United States

<sup>○</sup>Kavli Energy Nanoscience Institute, Berkeley, California 94720, United States

## S Supporting Information



**ABSTRACT:** The generation of chemical fuel in the form of molecular  $H_2$  via the electrolysis of water is regarded to be a promising approach to convert incident solar power into an energy storage medium. Highly efficient and cost-effective catalysts are required to make such an approach practical on a large scale. Recently, a number of amorphous hydrogen evolution reaction (HER) catalysts have emerged that show promise in terms of scalability and reactivity, yet remain poorly understood. In this work, we utilize Raman spectroscopy and X-ray absorption spectroscopy (XAS) as a tool to elucidate the structure and function of an amorphous cobalt sulfide ( $CoS_x$ ) catalyst. *Ex situ* measurements reveal that the as-deposited  $CoS_x$  catalyst is composed of small clusters in which the cobalt is surrounded by both sulfur and oxygen. *Operando* experiments, performed while the  $CoS_x$  is catalyzing the HER, yield a molecular model in which cobalt is in an octahedral  $CoS_2$ -like state where the cobalt center is predominantly surrounded by a first shell of sulfur atoms, which, in turn, are preferentially exposed to electrolyte relative to bulk  $CoS_2$ . We surmise that these  $CoS_2$ -like clusters form under cathodic polarization and expose a high density of catalytically active sulfur sites for the HER.

## INTRODUCTION

Due to the intermittency of sunlight and temporal mismatch between maximum solar photon flux and peak power consumption, it is necessary to convert sunlight into an energy storage medium.<sup>1</sup> The production of  $H_2$  via water electrolysis is a method of doing so that has attracted much attention, yet still faces numerous challenges.<sup>2–4</sup> One such limitation is the prohibitive cost of commonly used Pt hydrogen evolution reaction (HER) catalysts. Recently, a number of earth abundant HER catalysts have emerged in the form of amorphous transition metal chalcogenides that exhibit high catalytic

activity, scalability, and low cost that renders them attractive candidates to replace Pt in water electrolyzer systems and photoelectrochemical cells.<sup>5–11</sup> However, these materials are poorly understood and the origins behind their remarkable catalytic efficiency remain elusive.

Despite the difficulty in characterizing these promising, yet not well understood catalysts, significant progress has been made over the past decade through the use of *operando*

Received: April 5, 2015

Published: June 8, 2015

spectroscopic techniques. Investigations of amorphous HER and oxygen evolution reaction (OER) catalysts yield a common trend in which catalysts transform from a resting state to a catalytically active state which is quite different in terms of local atomic structure, oxidation state, or chemical composition. For example, an amorphous manganese oxide bifunctional OER and oxygen reduction reaction (ORR) catalyst was studied using X-ray absorption spectroscopy (XAS) and was shown to exist in three distinct atomic arrangements and average oxidation states, depending on the potential applied to the catalyst.<sup>12</sup> Moreover, electrodeposited amorphous molybdenum sulfide catalysts exhibiting significantly higher catalytic activities than bulk MoS<sub>2</sub> were examined with in situ X-ray photoelectron spectroscopy (XPS) and XAS.<sup>13–15</sup> The amorphous materials were found to be composed of a mixture of MoS<sub>3</sub> and MoO<sub>x</sub> that formed a surface layer of MoS<sub>2</sub> with a high active site density under cathodic polarization that was believed to be responsible for the catalytic HER activity. Another study demonstrated that increases in the OER catalytic activity of amorphous Ni–borate OER catalysts were accompanied by changes in Ni oxidation state and transformation into  $\gamma$ -NiOOH like molecular clusters.<sup>16</sup> These aforementioned works, in addition to multiple others, have yielded crucial structure–function relationships that are aiding both next generation catalyst design and understanding of fundamental chemistry.<sup>17</sup>

Within this context, we identified an amorphous cobalt sulfide (CoS<sub>x</sub>) HER catalyst recently developed in our lab as a worthwhile system to investigate its structure and function.<sup>6</sup> The CoS<sub>x</sub> HER catalyst requires only 83 mV overpotential to reach an operating current of 2 mA/cm<sup>2</sup> and is more active than many molybdenum sulfide catalysts, rendering it an intriguing, yet largely unknown system to study (Supporting Information Table S1). To perform such an analysis, we utilize a variety of spectroscopic tools to gain insight into the composition, local atomic structure, and catalytic activity of CoS<sub>x</sub>. In the following sections, we show through primarily Raman and X-ray absorption spectroscopies that CoS<sub>x</sub> exhibits a transient behavior, in which cobalt oxide and sulfide clusters spontaneously transform into CoS<sub>2</sub>-like molecular domains with a high sulfur active site density under HER operating conditions. We stress that the XAS and Raman measurements are conducted in true *operando* conditions that are identical to those of the CoS<sub>x</sub> electrochemical testing.

## RESULTS AND DISCUSSION

The CoS<sub>x</sub> catalyst is synthesized through a simple electrodeposition procedure, in which a conductive substrate is cycled between negative and positive potentials in a precursor electrolyte solution (Figure 1a). Cobalt chloride and thiourea serve as cobalt and sulfur precursors, respectively, in a pH 7 aqueous phosphate buffered electrolyte. Beginning the cycle at −1.2 V versus Ag/AgCl, the cyclic voltammogram (CV) initially shows an anodic peak at −0.3 V versus Ag/AgCl, which is attributed to the oxidation of aqueous divalent cobalt ions.<sup>18,19</sup> When scanning in the negative direction, a cathodic peak arises and is likely due to the reduction and coprecipitation of cobalt and sulfur and formation of the CoS<sub>x</sub> film. Control experiments (Supporting Information Figure S1) that performed the CV cycles in a phosphate buffer containing only thiourea showed neither anodic nor cathodic peaks, while CV cycles in a phosphate buffer/cobalt chloride solution exhibited only the first anodic peak. The Raman

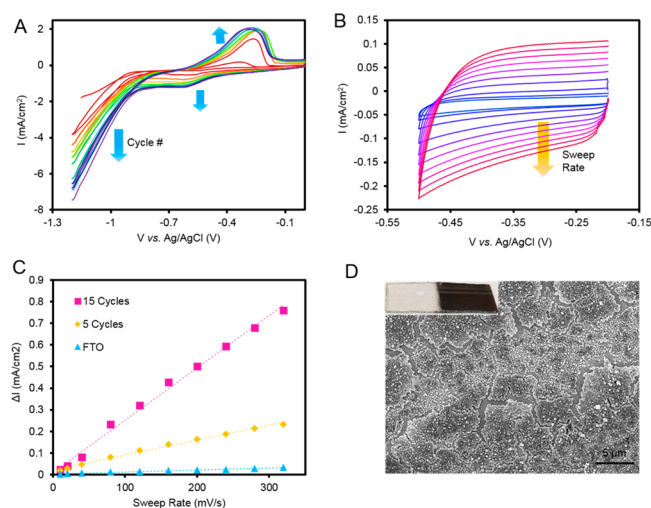


**Figure 1.** CoS<sub>x</sub> catalyst is electrodeposited through a series of CV sweeps (A) A typical voltammogram shows an anodic peak at −0.3 V versus Ag/AgCl, a cathodic peak at −0.5 V versus Ag/AgCl, and a cathodic current at potentials more negative than −0.7 V versus Ag/AgCl, which increases with increasing number of CV cycles. Electrochemical double layer capacitance (B and C) indicates that the CoS<sub>x</sub> film after 5 and 15 cycles of electrodeposition possesses a surface area of 8 and 23 times higher than the bare FTO substrate. An SEM image of the CoS<sub>x</sub> film (d) shows a rough, cracked surface. Optically, the film has a reflective black appearance (inset).

spectra of the resulting electrodes revealed only the presence of thiourea and cobalt oxide, respectively (Supporting Information Figure S2). The cathodic current at potentials more negative than −0.7 V versus Ag/AgCl is attributed to the HER. As an increasing number of CV cycles is performed and consequently, a thicker CoS<sub>x</sub> layer is deposited on the electrode, the HER current increases (Supporting Information Figure S3). This observation provides evidence for the electrodeposition of a porous CoS<sub>x</sub> film with HER active sites exposed not only at the surface but also throughout the film depth. If only the CoS<sub>x</sub> film surface was catalytically active, the HER current with each CV cycle would remain relatively constant or decrease from an increased CoS<sub>x</sub> film series resistance. Additional evidence for the porous nature of the film is provided by electrochemical double layer capacitance measurements. This measurement is conducted by recording capacitive current as a function of voltage sweep rate in a non-Faradaic potential region, which gives a first order approximation of the electrochemically active surface area.<sup>20,21</sup> The results of this measurement, shown in Figure 1b,c, indicate that the CoS<sub>x</sub> films from 5 and 15 electrodeposition cycles have roughness factors, defined as the ratio of electrochemically accessible surface area to projected surface area, of 8 and 23 relative to the bare fluorine-doped tin oxide (FTO) substrate on which the CoS<sub>x</sub> film is deposited. The as-deposited film shows a rough surface with cracks present throughout when observed using scanning electron microscopy (SEM) (Figure 1d). Energy dispersive spectroscopy (EDS) indicates that the film has a uniform Co/S ratio of 1.4:1.0. Macroscopically, the CoS<sub>x</sub> has a shiny black appearance as shown in the inset of Figure 1d, for a CoS<sub>x</sub> film deposited on conductive FTO coated glass. A final annealing step under argon atmosphere at 300 °C is performed before measurements. X-ray diffraction (XRD) of the CoS<sub>x</sub> films presents no noticeable peaks other than those from the conductive substrate and only a broad background is observed.<sup>6</sup> Such an

absence of diffraction peaks aside from those due to the substrate indicates the lack of significant long-range crystalline order.

We next use Raman spectroscopy to obtain an initial picture of the as-made catalyst composition and structure. Raman spectroscopy has proved to be an invaluable tool in materials characterization.<sup>22,23</sup> This type of vibrational spectroscopy analyzes inelastically scattered light in which the energy lost is used to excite molecular vibrations that feature a change in polarizability. A representative Raman spectrum of the  $\text{CoS}_x$  catalyst is presented in Figure 2. Peaks at 682, 612, 518, 473,

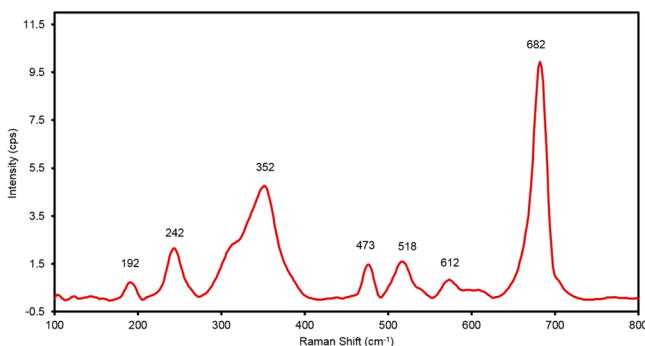


**Figure 2.** A typical Raman spectrum of the as-made  $\text{CoS}_x$  film exhibits  $\text{CoO}/\text{Co}_3\text{O}_4$  and  $\text{Co}(\text{OH})_2$  peaks, as well as a broad peak at  $352\text{ cm}^{-1}$ .

and  $192\text{ cm}^{-1}$  are attributed to  $\text{CoO}$  or  $\text{Co}_3\text{O}_4$ , while the peak at  $242\text{ cm}^{-1}$  is attributed to  $\text{Co}(\text{OH})_2$ .<sup>24–26</sup> These peak positions are consistent with both the literature values and our own spectra on standard  $\text{CoO}$ ,  $\text{Co}_3\text{O}_4$ , and  $\text{Co}(\text{OH})_2$  powders (Supporting Information Figure S4). The broad peak at  $352\text{ cm}^{-1}$  cannot be matched to any standard nor to any well-characterized  $\text{Co-S}$  phase, yet lies in the wavenumber region where many transition metal sulfides exhibit Raman peaks and is tentatively attributed to a  $\text{Co-S}$  vibration. The oxide fraction in the  $\text{CoS}_x$  likely forms upon exposure to air and its presence is not surprising, given that cobalt metal readily oxidizes in air and a porous, disordered film would likely have an even greater propensity to be at least partially oxidized. Depth-resolved X-ray photoelectron spectroscopy (XPS) (Supporting Information Figure S5) indicates that an oxide is present throughout the entire thickness of the film, with the surface having similar chemical composition as the bulk. This is further evidence that the film is porous in nature, and a  $\text{CoS}_x$ -air interface exists throughout the entire film thickness.

The electronic structure and local chemical environment of the  $\text{CoS}_x$  film are probed with X-ray absorption near edge spectroscopy (XANES). For each XANES region, spectra of several standards are acquired and used as a basis for comparison. Cobalt K-edge XANES, which probes primarily the  $1s-4p$  transitions (Figure 3a), serves as a qualitative spectroscopic fingerprint to aid in identification of the cobalt species present in our film.<sup>27–30</sup> Cobalt oxides have an intense white line, while cobalt sulfide has a much broader absorption edge, even though cobalt in these sulfides possesses the same oxidation state as  $\text{CoO}$  and  $\text{Co}(\text{OH})_2$ . Qualitatively, the  $\text{CoS}_x$  has a Co K-edge structure that resembles a mixture of an oxide and sulfide material. Co L-edge XANES offers a more quantitative determination of oxidation state, which is proportional to the area under the  $\text{Co L}_3$  edge.<sup>31–34</sup> Analyzing the  $\text{CoS}_x$  white line area after normalizing the pre- and post-edge to 0 and 1, respectively (Supporting Information Figure S7),

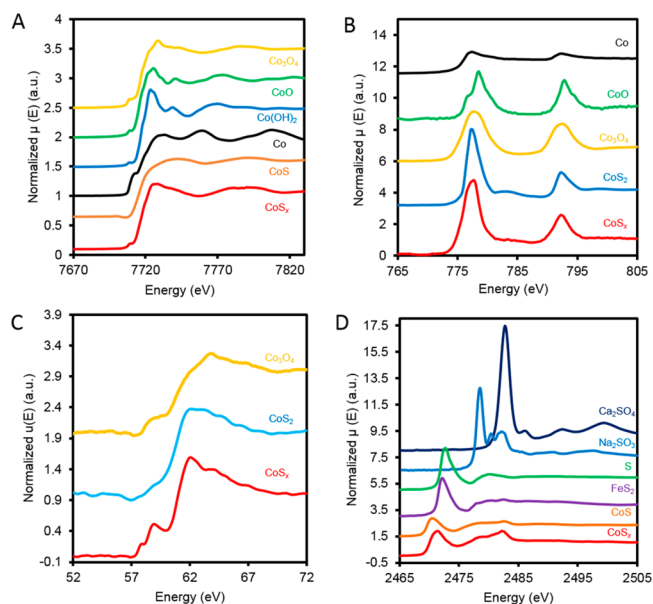


**Figure 3.** XANES characterization of  $\text{CoS}_x$ . (A) Co K-edge spectra indicate both oxide and sulfide characteristics in the  $\text{CoS}_x$  spectral line shape. (B) The average oxidation state is confirmed to be  $\text{Co}^{2+}$  from L-edge analysis. (C) Co M-edge absorption spectroscopy further indicate oxide and sulfide character simultaneously present, (D) while the S is determined from S K-edge to be sulfide-like with an average oxidation state of  $\text{S}^{1.5-}$ .

reveals an average oxidation state of  $2+$  for the cobalt in  $\text{CoS}_x$  (Figure 3b), consistent with previous XPS analysis.<sup>6</sup>

Transition metal M-edge spectroscopy is an emerging materials characterization tool that utilizes extreme ultraviolet (XUV) photons to probe  $3p-3d$  transitions.<sup>35–38</sup> The M-edge line shape can reveal oxidation state, ligand field and spin state of the probed transition metal that arises from coulomb and exchange coupling between the  $3d$  electrons and  $3p$  core hole. We compared the static XUV absorption of  $\text{CoS}_x$ ,  $\text{Co}_3\text{O}_4$ , and  $\text{CoS}_2$ . Qualitatively, the  $\text{CoS}_x$  spectra have features associated with both oxide and sulfides. The pre-edge feature at  $58\text{ eV}$  and rising edge at  $61\text{ eV}$  have previously been assigned to  $\text{Co}^{2+}$  ions.<sup>37</sup> The M-edge position in the  $\text{CoS}_x$  spectrum suggests that the main oxidation state of cobalt is  $\text{Co}^{2+}$ , unlike  $\text{Co}_3\text{O}_4$ , which is a  $1:2$  mixture of  $\text{Co}^{2+}$  and  $\text{Co}^{3+}$  and has relatively more absorption features at higher energies.

The sulfur component in the  $\text{CoS}_x$  films is next studied with S K-edge XANES. For sulfur compounds, the peak energy is proportional to sulfur oxidation state, which can range from  $2471\text{ eV}$  for  $\text{S}^{2-}$  to  $2483\text{ eV}$  for  $\text{S}^{6+}$ .<sup>39–41</sup> The S K-edge peak position for  $\text{CoS}_x$  indicates that the sulfur has an average oxidation state of  $-1.5$ . Taken together, XANES analysis of  $\text{CoS}_x$  Co K, Co L, Co M, and S K-edges presents a picture of a partially oxidized amorphous cobalt sulfide. The EDS Co/S ratio of  $1.4:1.0$  would have cobalt in excess for any of the main cobalt sulfide phases and it is likely that the excess Co is present in the form of an oxide.

Ex situ experiments yield valuable information on the chemical nature of  $\text{CoS}_x$ , yet the origin of high catalytic activity in this film remains largely unknown. To address this issue, analogous *operando* experiments are performed on the same catalyst. Raman spectroscopy is first utilized as a spectroscopic means of observing any structural changes that may occur during HER reaction conditions. At open circuit conditions, the



same spectral features as those on the as-made catalyst are observed (Figure 4a). As the  $\text{CoS}_x$  electrode potential is

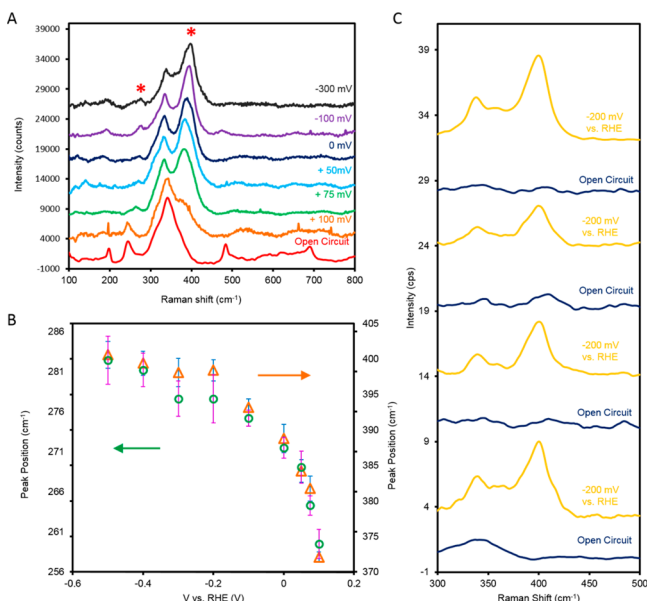


**Figure 4.** Operando Raman spectroscopy of  $\text{CoS}_x$ . With increasingly negative potentials, two new peaks arise that are attributed to the formation of  $\text{CoS}_2$ -like domains (A). These peaks blue-shift with increasing negative potential (B), potentially indicative of bond-strengthening. Orange triangles represent the  $\text{CoS}_2$   $A_g$ -like peak and green circles represent the  $\text{CoS}_2$   $E_g$ -like peak. The  $\text{CoS}_2$ -like mode appearance is reversible and is maintained through multiple cycles (C). The bottom spectrum represents the 1st Raman spectrum of the  $\text{CoS}_x$  film and the top represents the last.

systematically increased in the cathodic direction (more negative versus the reversible hydrogen electrode, (RHE)), new peaks in the Raman spectrum appear at 260 and 370  $\text{cm}^{-1}$ . The catalyst was held at the desired potential for 5 min before acquiring each spectrum to reach steady state conditions. The peaks previously attributed to  $\text{CoO}/\text{Co}_3\text{O}_4$  disappear and the peak at 352  $\text{cm}^{-1}$  remains constant. These changes initially become noticeable at +100 mV versus RHE and seem to occur within the 5 min time frame after applying a cathodic potential. An initial explanation for the disappearance of the oxide is drawn from the cobalt–oxygen Pourbaix diagram, where at pH 7 the thermodynamically preferred state of cobalt transitions from  $\text{Co}^{2+}$  to metallic Co at a potential slightly positive of RHE.<sup>19</sup> As the potential of the electrode is shifted to more negative potentials, the two new peaks grow in intensity and dominate the Raman spectrum. These two peaks have the same Raman shift as the  $A_g$  and  $E_g$  modes of  $\text{CoS}_2$ , although their full width at half-maximum intensity (FWHM) is 30  $\text{cm}^{-1}$ , which is roughly twice that of crystalline  $\text{CoS}_2$  (Supporting Information Figure S8).<sup>42–44</sup> This line broadening is indicative of a disordered material or small cluster size.<sup>43–47</sup>

To the best of our knowledge, no experimentally or theoretically determined cobalt–sulfur Pourbaix diagram exists. However, one can draw analogy to the iron–sulfur Pourbaix diagram, where at pH 7 the  $\text{FeS}_2$  pyrite phase becomes thermodynamically preferred at +300 mV versus RHE.<sup>48,49</sup> The  $\text{CoS}_2$  Raman signature observed in combination with previous electrochemical studies on analogous transition metal sulfide systems suggests that the  $\text{CoS}_x$  is spontaneously transforming

into  $\text{CoS}_2$ -like microdomains under cathodic polarization. One observation of note is the blueshift of the  $\text{CoS}_2$ -like Raman peaks with increasingly negative potential (Figure 4b). Potential-dependent Raman redshifts are commonly observed in adsorbed molecules whose bonds are weakened or vice versa where bonds are being strengthened from an electrochemical process.<sup>50–53</sup> Changes in electronic density have also been attributed to potential-dependent Raman shifts.<sup>54–56</sup> The blueshift in our case suggests the possible strengthening of Co–S bonds with increasingly negative potential. This  $\text{CoS}_2$ -like phase is stable only under reducing potentials, and upon the return to open circuit, the Raman spectrum resembles that of cobalt hydroxide with the majority of the  $\text{CoS}_2$  signal gone. This change is reversible for multiple cycles of switching between cathodic polarization and open circuit conditions (Figure 4c) though a small peak at 390  $\text{cm}^{-1}$  remains 5 min after applying a negative potential, when the next spectrum at open circuit is taken.

Complementary *operando* X-ray absorption experiments are performed to more completely understand the structure of the  $\text{CoS}_x$  catalyst during reaction conditions. From the dry sample to that immersed in electrolyte in open circuit conditions, there is minimal change in the near edge spectrum (Figure 5a),

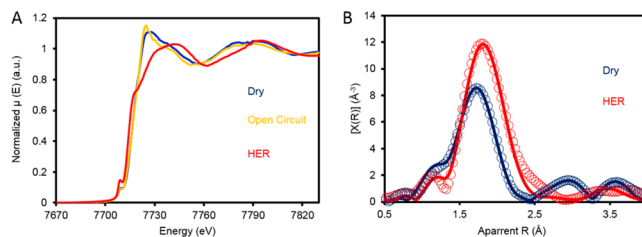


**Figure 5.** Operando Co K-edge XANES (A) reveals a line shape change that suggests transformation from cobalt oxide to cobalt sulfide. EXAFS (B) qualitatively indicates an increased average bond length and decreased shell contributions. Open circles represent the experimental data and solid lines represent the fit.

except for a slightly sharper white line characteristic of  $\text{Co}(\text{OH})_2$  (*vide supra*). However, under an applied potential of −150 mV versus RHE, the Co K-edge white line disappears and the spectrum resembles that of a transition metal sulfide.<sup>27</sup> The disappearance of the oxide and formation of a cobalt sulfide species is consistent with the *operando* Raman data. The increase in intensity of the pre-edge peak, a dipole-forbidden  $1s \rightarrow 3d$  transition, indicates increased p–d orbital mixing, which can be explained by an increased p–d hybridization in cobalt sulfides relative to oxides.<sup>57–59</sup> Linear combination fitting of XANES data using the spectra of reference compounds is performed to obtain a first-order approximation of the  $\text{CoS}_x$  catalyst under dry and HER conditions. Through linear combination fitting, the best fits yielded a composition of 60% CoO and 40% CoS in the dry state and 26% CoO and 74% CoS under HER conditions. Operando Co L-edge XANES reveals that the oxidation state remains at +2, but features a satellite peak increase that is also attributed to p–d hybridization (Supporting Information Figure S9).<sup>27,60–62</sup> Likewise, the S K-edge spectrum remains consistent from open circuit conditions to reducing potentials (Supporting Information Figure S10), indicating that the sulfur has a similar oxidation state throughout the process and the overall change to  $\text{CoS}_2$  microdomains affects the Co K-edge more than the S K-edge.

XANES data is an important tool for oxidation state analysis and qualitative spectroscopic fingerprint comparison, yet quantitative information about the immediate chemical surroundings of the investigated element is difficult to extract due to multiple scattering processes and bound to bound transitions. To this end, we utilize extended X-ray absorption fine structure (EXAFS) analysis to obtain such information. In essence, the EXAFS phenomenon is the modulation of the X-ray absorption coefficient of the absorbing atom due to constructive or destructive interference of the forward propagating and backscattered waves of the ejected photoelectron due to scattering by neighboring atoms.<sup>63–65</sup> By analyzing the fine structure of the X-ray absorption spectrum, quantitative information about coordination number, coordination atoms, bond lengths, and structural disorder can be obtained. We analyze the EXAFS spectra for two samples: an as-made  $\text{CoS}_x$  film and the same  $\text{CoS}_x$  film operating at reaction conditions at  $-150$  mV versus RHE. The Fourier transform EXAFS spectra for  $\text{CoS}_x$  are plotted in R-space in Figure 5b. A qualitative assessment of the two spectra reveals two main differences between the as-made and *operando* samples. (1) Upon cathodic polarization, the average bond length increases slightly and (2) the second shell contribution decreases significantly. Co–S bonds are typically  $\sim 12\%$  longer than Co–O bonds and the increase in average bond length points to an increase in the fraction of Co–S bonds in the  $\text{CoS}_x$  film. Compared to  $\text{CoO}$ ,<sup>66</sup> the dry  $\text{CoS}_x$  film has significantly weaker features beyond the first shell and these features further decrease in intensity under HER catalytic conditions, indicative of Co–S clusters that are mainly composed of Co surrounded by a single shell of S with little ordering beyond this first shell. Since the dry film is partially oxidized and likely more ordered, we see an increased amplitude in the second and third shells in the EXAFS data.

Quantitative analysis is performed by modeling the EXAFS spectra. Due to experimental evidence for the presence of  $\text{CoO}$  and  $\text{CoS}_2$  as the main cobalt species present (*vide supra*), these two structures were used as initial models to fit the  $\text{CoS}_x$  experimental EXAFS data.  $\text{CoO}$  and  $\text{CoS}_2$  both have Co surrounded by octahedral O and S, respectively. Complete fitting parameters and results can be found in the Supporting Information. A best fit of the dry  $\text{CoS}_x$  film yields a combination of octahedral Co atom that has on average 2.1 O atoms and 2.1 S atoms in the first shell. Second shell scattering paths with a coordination number approximately half that of bulk  $\text{CoO}$  and  $\text{CoS}_2$  are fit to the data. The second shell paths give evidence for a slight phase segregation of cobalt oxide and sulfide into these sub-nanometer clusters as opposed to a homogeneous cobalt oxysulfide material. Data modeling utilizing only one crystal structure ( $\text{CoO}$ ,  $\text{Co}_3\text{O}_4$ ,  $\text{Co}_9\text{S}_8$ , or  $\text{CoS}_2$ ) did not yield a reasonable fit.

A best fit for the *operando*  $\text{CoS}_x$  film features the Co surrounded by 5.2 S atoms and 0.8 O atoms, which serves as further confirmation of the *operando* oxide–sulfide transformation. Second shell Co–S scattering paths have minimal contributions to the EXAFS fit likely due to the material disorder or relatively poor scattering ability of sulfur, while Co–Co scattering contributions in the second shell are fit to give a coordination of  $\sim 3$ , suggesting that the *operando*  $\text{CoS}_x$  film consists of few-nuclei  $\text{CoS}_2$  clusters.

Completely omitting the oxide fraction from the model results in a significantly poorer fit (a misfit of 8.5% versus 1.3%, Supporting Information Figure S13), suggesting that there

is a small oxide fraction remaining within the film, even under HER operating conditions. This oxide fraction may not be in electrical contact with the conductive substrate and therefore does not transform into  $\text{CoS}_2$ -like clusters. However, after electrolysis for 3 h, the Co:S ratio, as measured by EDS, decreases from 1.4:1 to 0.98:1, indicating that a fraction of the cobalt dissolves into the electrolyte. This is consistent with the formation of  $\text{CoS}_2$ -like clusters under HER operating conditions since the sulfur content would be the stoichiometrically limiting reagent and some of the remaining cobalt is likely to dissolve away.

From a comprehensive data set utilizing information from Raman, XANES, and EXAFS, an atomic structural model of the *operando* state of  $\text{CoS}_x$  emerges (Figure 6). Immediately

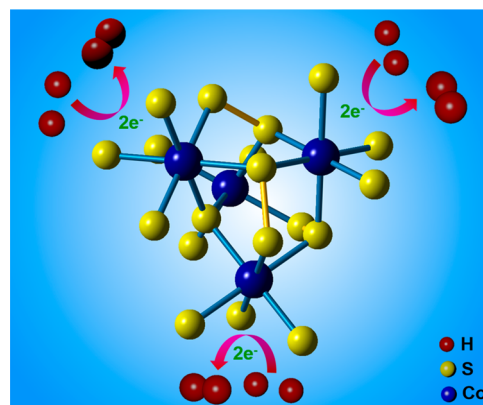


**Figure 6.** Atomic model of  $\text{CoS}_x$  catalyst derived from Raman, XANES, and EXAFS data.

noticeable are the undercoordinated sulfur atoms on the perimeter of the  $\text{CoS}_x$  cluster. *Operando* XANES determines the sulfur species to be sulfide-like even at open circuit conditions; therefore, their oxidation to sulfates upon exposure to electrolyte is not likely. *Operando* Raman measurements indicate the presence of a disordered  $\text{CoS}_2$ -like molecular cluster state. This state is confirmed through XANES and EXAFS as being the predominant form of cobalt. EXAFS analysis reveals a near complete octahedral shell of S around the central Co and partial second shell contribution of 3 additional Co atoms yielding the best fit, giving a cluster size of several cobalt nuclei. A small molecular  $\text{CoS}_2$ -like cluster is rendered in Figure 6. Additional renditions of the structural model are presented in the Supporting Information.

Transition and precious metal disulfides such as  $\text{MoS}_2$ ,  $\text{CoS}_2$ , and  $\text{RuS}_2$  were well-studied hydrodesulfurization (HDS) catalysts before drawing attention for their HER catalytic functionality.<sup>67–73</sup> For  $\text{MoS}_2$ , edge sites featuring undercoordinated S atoms were ascertained to be the primary HDS active sites and in recent years, the same sites were determined to also be the active sites for the HER reactions.<sup>74</sup> From the onset of this discovery, many efforts have been put forth to engineer  $\text{MoS}_2$  catalysts to feature an abundance of active sites and have resulted in significant improvements of  $\text{MoS}_2$  catalytic efficiencies.<sup>75–78</sup>

It is plausible that disulfide anions ( $\text{S}_2^{2-}$ ) play a similar role in the HER reaction on  $\text{CoS}_2$  surfaces and initial reports have suggested likewise. Transition metal chalcogenides and crystalline pyrite materials, especially  $\text{CoS}_2$ , have been previously demonstrated to be highly active HER catalysts.<sup>79–82</sup>

The density of exposed sulfide atoms, presumably the active sites for the HER, on a microscopic level has been linked to the catalysts' performance. Within this context, the *operando* CoS<sub>x</sub> atomic model is an ideal structure for a CoS<sub>2</sub> based catalyst, because a significant fraction of S atoms are accessible for catalysis. The high catalytic activity observed for these amorphous films relative to crystalline CoS<sub>2</sub> might be explained by this high density of exposed active sites and possible electronic differences between these molecular clusters and the bulk pyrite structure, which warrants further study.

## CONCLUDING REMARKS

In summary, a highly active CoS<sub>x</sub> catalyst is investigated through an *operando* spectroscopic approach. Through a combination of Raman and XAS experiments, we find that the as-made CoS<sub>x</sub> consists of a porous amorphous film composed of small oxide and sulfide clusters. Upon the application of cathodic polarization, the CoS<sub>x</sub> catalyst transforms into CoS<sub>2</sub>-like molecular clusters. We speculate that the origins of high HER activity lie in the presence of a high density of accessible sulfur atoms along the cluster periphery, which might exhibit different binding strength relative to the active sites in bulk CoS<sub>2</sub>.

## EXPERIMENTAL SECTION

### CoS<sub>x</sub> Electrodeposition and Electrochemical Measurements.

All electrochemical measurements were performed with a Biologic VMP 300 potentiostat and EC-Lab software. The CoS<sub>x</sub> film was electrodeposited from a solution of 0.5 M thiourea and 5 mM CoCl<sub>2</sub> in a 0.5 M, pH 7, phosphate buffer. Between 5 and 50 electrodeposition cycles were carried on a conductive substrate. Ag/AgCl and FTO were used as reference and counter electrodes, respectively. Cyclic voltammetry was carried out at a 5 mV/second sweep rate, sweeping from −1.2 V versus Ag/AgCl to +0.2 V versus Ag/AgCl. After electrodeposition, the CoS<sub>x</sub> film was rinsed thoroughly with deionized water. Before electrochemical measurements, an annealing step was carried out at 300 °C for 2 h in an argon environment. For all electrochemical measurements, the electrolyte was sparged with argon gas for 30 min to remove dissolved oxygen.

**Electron Microscopy.** Scanning electron microscopy images were collected with a JEOL 6340 FESEM operating at a 5 kV accelerating voltage and 6 mm working distance. EDS elemental spectra were acquired under 20 kV accelerating voltage at a 15 mm working distance with TEAM EDAX analysis hardware/software.

**X-ray Photoelectron Spectroscopy.** XPS spectra were acquired with a PHI 5400 X-ray photoelectron spectrometer equipped with a 4 kV argon ion gun and Al K $\alpha$  radiation. The angle between the source and detector was 35°. The measurement chamber was maintained at  $\sim 10^{-9}$  Torr ( $\sim 10^{-7}$  Pa) during measurement, and measurements were taken at pass energy of 17.9 eV. All energies were calibrated to spurious carbon at 285.0 eV.

**Raman Spectroscopy.** Raman spectroscopy was carried out with a Horiba Jobin-Vyon Labram HR 800 Micro-Raman instrument and Labspec software. All Raman spectra were acquired with 532 nm excitation from a 250 mW diode laser. The incident laser power was decreased by a factor of 100 to avoid sample damage. *Operando* Raman spectroscopy was carried out in a home-built open spectroelectrochemical cell with Ag/AgCl and titanium foil as reference and counter electrodes, respectively. The electrolyte used was a 0.5 M phosphate buffered pH 7 aqueous solution. Acquisition of spectra at steady-state conditions was performed after holding the catalyst at the desired potential for 5 min. Each acquisition took between 5 and 10 min.

**X-ray Absorption Measurements.** All XAS measurements were conducted at the Advanced Light Source at Lawrence Berkeley National Lab with an electron energy of 1.9 GeV and current of 500 mA. Co K-edge and S K-edge experiments were performed at

beamline 10.3.2, Co L-edge experiments were performed at beamline 6.3.1.2. Energy calibration was performed using a glitch in the incident intensity,  $I_0$ , relative to a cobalt foil or calcium sulfate standard for K-edge data acquisition. L-edge data was calibrated relative to a cobalt foil standard. M-edge spectra were collected on 10 nm thin films of the desired material deposited on 100 nm thick silicon nitride membranes. To minimize the absorption of the incident photons, the measurements were conducted in a home-built vacuum chamber, held at  $10^{-7}$  Torr ( $\sim 10^{-5}$  Pa). The incident photon spot is raster scanned along the sample to avoid any possible sample damage and degradation. *Operando* XAS experiments were conducted using home-built spectroelectrochemical cells. The cells were constructed of a PEEK thermoplastic polyaryletherketone polymer body with small inlet ports for gases, Ag/AgCl reference electrodes, and Pt counter electrodes. Each *operando* measurement took between 2 and 4 h. The electrolyte used was a 0.5 M phosphate buffered pH 7 aqueous solution. The electrolyte compartment was separated from either an ambient or UHV ( $10^{-9}$  Torr) atmosphere through a 6  $\mu$ m thick Mylar film or with a 100 nm thick silicon nitride window. Diagrams of the electrochemical cells used are presented in the Supporting Information.

**X-ray Data Processing.** Near-edge data reduction was performed with commonly used Athena software to remove the pre- and post-edge contributions of the spectra and normalized the X-ray absorption coefficient. Linear combination fitting of XANES spectra was also performed with Athena software. EXAFS data was fit with Artemis, IFEFFIT and Feff 6 software.<sup>83–85</sup> Ab initio phases and amplitudes were used in the EXAFS equation to fit experimental data:

$$\chi(k) = S_0^2 \sum_i \frac{N_i}{kR_i^2} F_i(k) e^{-2\sigma_i^2 k^2} e^{-2R_i/\lambda_i k} \sin(2kR_i - \varphi_i(k))$$

Neighboring atoms are divided into  $i$  shells with coordination numbers  $N_i$  at a distance of  $R_i$  from the central atom. The amplitude function for each shell is denoted  $F_i(k)$ .  $S_0^2$  is the amplitude reduction factor and is intrinsic to the central atom, accounting for shakeup processes at the central atom. From a fit to a cobalt foil standard,  $S_0^2$  was taken to be 0.76 and kept constant in the EXAFS fitting of CoS<sub>x</sub>. The damping due to thermal or structural disorder is accounted for by the Debye–Waller term,  $e^{-2\sigma_i^2 k^2}$ . Amplitude losses due to inelastic scattering are factored in with the mean free path term,  $e^{-2R_i/\lambda_i k}$ , where  $\lambda_i$  is the photoelectron mean free path. The periodicity in the X-ray absorption coefficient is reflected in the sinusoidal term:  $\sin(2kR_i + \varphi_i(k))$ , where  $\varphi_i(k)$  is the phase function for the coordination shell,  $i$ . In the data fitting process,  $R_i$ ,  $N$ , and  $\sigma_i$  were floating variables, while other parameters were fixed.

## ASSOCIATED CONTENT

### Supporting Information

EXAFS fitting parameters, catalytic efficiency comparisons of hydrogen evolution catalysts, spectroscopic standards. The Supporting Information is available free of charge on the ACS Publications website at DOI: 10.1021/jacs.5b03545.

## AUTHOR INFORMATION

### Corresponding Author

\*p\_yang@berkeley.edu

### Notes

The authors declare no competing financial interest.

## ACKNOWLEDGMENTS

J.R. gratefully acknowledges the support of the National Science Foundation Graduate Research Fellowship Proposal (NSF GRFP) under Grant No. DGE-0802270. This work was supported by the Director, Office of Science, Office of Basic Energy Sciences, Materials Science and Engineering Division, U.S. Department of Energy under Contract No. DE-AC02-05CH11231(P-Chem). X-ray absorption experiments were



performed at the Advanced Light Source (ALS). The ALS is an Office of Science User Facility operated for the U.S. Department of Energy Office of Science by LBNL and supported by the U.S. Department of Energy under Contract No. DEAC02-05CH11231. We thank Dr. Sirine Fakra, Dr. Matthew Marcus, and Yi-De Chuang at the Advanced Light Source for help with XAS experiments.

## REFERENCES

- (1) Dresselhaus, M.; Thomas, I. *Nature* **2001**, *414*, 332.
- (2) Lewis, N. S.; Nocera, D. G. *Proc. Natl. Acad. Sci. U.S.A.* **2006**, *103*, 15729.
- (3) Faunce, T. A.; Lubitz, W.; Rutherford, W. A.; MacFarlane, D.; Moore, G. F.; Yang, P.; Nocera, D. G.; Moore, T. A.; Gregory, D. H.; Fukuzumi, S.; et al. *Energy Environ. Sci.* **2013**, *6*, 695.
- (4) Turner, J. A. *Science* **2004**, *305*, 972.
- (5) Merki, D.; Fierro, S.; Vrabel, H.; Hu, X. *Chem. Sci.* **2011**, *2*, 1262.
- (6) Sun, Y.; Liu, C.; Grauer, D. C.; Yano, J.; Long, J. R.; Yang, P.; Chang, C. J. *J. Am. Chem. Soc.* **2013**, *135*, 17699.
- (7) Carim, A. I.; Saadi, F. H.; Soriaga, M. P.; Lewis, N. S. *J. Mater. Chem. A* **2014**, *2*, 13835.
- (8) Jiang, N.; Bogoev, L.; Popova, M.; Gul, S.; Yano, J.; Sun, Y. *J. Mater. Chem. A* **2014**, *2*, 19407.
- (9) Morales-Guio, C. G.; Hu, X. *Acc. Chem. Res.* **2014**, *47*, 2671.
- (10) McEnaney, J. M.; Crompton, J. C.; Callejas, J. F.; Popczun, E. J.; Read, C. G.; Lewis, N. S.; Schaak, R. E. *Chem. Commun.* **2014**, *50*, 11026.
- (11) McEnaney, J. M.; Crompton, J. C.; Callejas, J. F.; Popczun, E. J.; Bicch, A. J.; Lewis, N. S.; Schaak, R. E. *Chem. Mater.* **2014**, *26*, 4826.
- (12) Gorlin, Y.; Lassalle-Kaiser, B.; Benck, J. D.; Gul, S.; Webb, S. M.; Yachandra, V. K.; Yano, J.; Jaramillo, T. F. *J. Am. Chem. Soc.* **2013**, *135*, 8525.
- (13) Casalongue, H. G. S.; Benck, J. D.; Tsai, C.; Karlsson, R. K.; Kaya, S.; Ng, M. L.; Pettersson, L. G.; Abild-Pedersen, F.; Nørskov, J.; Ogasawara, H.; et al. *J. Phys. Chem. C* **2014**, *118*, 29252.
- (14) Benck, J. D.; Chen, Z.; Kuritzky, L. Y.; Forman, A. J.; Jaramillo, T. F. *ACS Catal.* **2012**, *2*, 1916.
- (15) Lassalle-Kaiser, B.; Merki, D.; Vrabel, H.; Gul, S.; Yachandra, V. K.; Hu, X.; Yano, J. *J. Am. Chem. Soc.* **2015**, *137*, 314.
- (16) Bediako, D. K.; Lassalle-Kaiser, B.; Surendranath, Y.; Yano, J.; Yachandra, V. K.; Nocera, D. G. *J. Am. Chem. Soc.* **2012**, *134*, 6801.
- (17) Kanan, M. W.; Yano, J.; Surendranath, Y.; Dinca, M.; Yachandra, V. K.; Nocera, D. G. *J. Am. Chem. Soc.* **2010**, *132*, 13692.
- (18) Cui, C.; Jiang, S.; Tseung, A. J. *Electrochem. Soc.* **1990**, *137*, 3418.
- (19) Bajdich, M.; García-Mota, M.; Vojvodic, A.; Nørskov, J. K.; Bell, A. T. *J. Am. Chem. Soc.* **2013**, *135*, 13521.
- (20) Kötz, R.; Carlen, M. *Electrochim. Acta* **2000**, *45*, 2483.
- (21) Trasatti, S.; Petrii, O. J. *Electroanal. Chem.* **1992**, *327*, 353.
- (22) Colthup, N. *Introduction to Infrared and Raman Spectroscopy*; Academic Press: New York, 2012.
- (23) Long, D. A. *Raman Spectroscopy*; McGraw-Hill: New York, 1977.
- (24) Tang, C.-W.; Wang, C.-B.; Chien, S.-H. *Thermochim. Acta* **2008**, *473*, 68.
- (25) Yang, J.; Liu, H.; Martens, W. N.; Frost, R. L. *J. Phys. Chem. C* **2009**, *114*, 111.
- (26) Yeo, B. S.; Bell, A. T. *J. Am. Chem. Soc.* **2011**, *133*, 5587.
- (27) Mosselmans, J.; Patrick, R.; Van der Laan, G.; Charnock, J.; Vaughan, D.; Henderson, C.; Garner, C. *Phys. Chem. Miner.* **1995**, *22*, 311.
- (28) Binsted, N.; Cook, S. L.; Evans, J.; Greaves, G. N.; Price, R. J. *J. Am. Chem. Soc.* **1987**, *109*, 3669.
- (29) Sano, M. *Inorg. Chem.* **1988**, *27*, 4249.
- (30) Jiang, T.; Ellis, D. J. *Mater. Chem.* **1996**, *11*, 2242.
- (31) Charnock, J.; Henderson, C.; Mosselmans, J.; Patrick, R. *Phys. Chem. Miner.* **1996**, *23*, 403.
- (32) Nesvizhskii, A.; Rehr, J. J. *Synchrotron Radiat.* **1999**, *6*, 315.
- (33) De Groot, F.; Fuggle, J.; Thole, B.; Sawatzky, G. *Phys. Rev. B* **1990**, *42*, 5459.
- (34) Liu, H.; Guo, J.; Yin, Y.; Augustsson, A.; Dong, C.; Nordgren, J.; Chang, C.; Alivisatos, P.; Thornton, G.; Ogletree, D. F. *Nano Lett.* **2007**, *7*, 1919.
- (35) Van der Laan, G. *J. Phys.: Condens. Matter* **1991**, *3*, 7443.
- (36) Vura-Weis, J.; Jiang, C.-M.; Liu, C.; Gao, H.; Lucas, J. M.; de Groot, F. M.; Yang, P.; Alivisatos, A. P.; Leone, S. R. *J. Phys. Chem. Lett.* **2013**, *4*, 3667.
- (37) Jiang, C.-M.; Baker, L. R.; Lucas, J. M.; Vura-Weis, J.; Alivisatos, A. P.; Leone, S. R. *J. Phys. Chem. C* **2014**, *118*, 22774.
- (38) Adam, R.; Grychtol, P.; Cramm, S.; Schneider, C. *J. Electron Spectrosc. Relat. Phenom.* **2011**, *184*, 291.
- (39) Jalilehvand, F. *Chem. Soc. Rev.* **2006**, *35*, 1256.
- (40) Fleet, M. E.; Liu, X.; Harmer, S. L.; King, P. L. *Can. Mineral.* **2005**, *43*, 1605.
- (41) Farrell, S. P.; Fleet, M. E.; Stekhin, I. E.; Kravtsova, A.; Soldatov, A. V.; Liu, X. *Am. Mineral.* **2002**, *87*, 1321.
- (42) Lyapin, S.; Utyuzh, A.; Petrova, A.; Novikov, A.; Lograsso, T.; Stishov, S. *J. Phys.: Condens. Matter* **2014**, *26*, 396001.
- (43) Anastassakis, E.; Perry, C. J. *Chem. Phys.* **1976**, *64*, 3604.
- (44) Zhu, L.; Susac, D.; Teo, M.; Wong, K.; Parsons, R.; Bizzotto, D.; Mitchell, K.; Campbell, S. J. *Catal.* **2008**, *258*, 235.
- (45) Nakamura, K.; Fujitsuka, M.; Kitajima, M. *Phys. Rev. B* **1990**, *41*, 12260.
- (46) Gouadec, G.; Colomban, P. *Prog. Cryst. Growth Charact. Mater.* **2007**, *53*, 1.
- (47) Ganan, N. J. *Raman Spectrosc.* **2005**, *36*, 879.
- (48) Sandström, M.; Jalilehvand, F.; Persson, L.; Gelius, U.; Frank, P.; Hall-Roth, I. *Nature* **2002**, *415*, 893.
- (49) Mcneil, M. B.; Little, B. J. *J. Am. Inst. Conserv.* **1992**, *31*, 355.
- (50) Oklejas, V.; Harris, J. M. *Appl. Spectrosc.* **2004**, *58*, 945.
- (51) Roy, D.; Furtak, T. J. *Chem. Phys.* **1984**, *81*, 4168.
- (52) Weaver, M. J.; Farquharson, S.; Tadayoni, M. *J. Chem. Phys.* **1985**, *82*, 4867.
- (53) Weaver, M. J.; Hupp, J. T.; Barz, F.; Gordon, J. G.; Philpott, M. R. *J. Electroanal. Chem. Interfacial Electrochem.* **1984**, *160*, 321.
- (54) Corio, P.; Santos, P.; Brar, V.; Samsonidze, G. G.; Chou, S.; Dresselhaus, M. *Chem. Phys. Lett.* **2003**, *370*, 675.
- (55) Rao, A. M.; Eklund, P.; Bandow, S.; Thess, A.; Smalley, R. E. *Nature* **1997**, *388*, 257.
- (56) Han, X. X.; Köhler, C.; Kozuch, J.; Kuhlmann, U.; Paasche, L.; Sivanesan, A.; Weidinger, I. M.; Hildebrandt, P. *Small* **2013**, *9*, 4175.
- (57) Pavlov, N.; Galkin, V.; Nekrasov, I.; Kurmaev, E. *Phys. Solid State* **2009**, *51*, 2207.
- (58) Bullett, D. J. *Phys. C: Solid State Phys.* **1982**, *15*, 6163.
- (59) Flory, M.; McLamarras, S.; Ziurys, L. J. *Chem. Phys.* **2005**, *123*, 164312.
- (60) Muro, T.; Kimura, A.; Iwasaki, T.; Ueda, S.; Imada, S.; Matsushita, T.; Sekiyama, A.; Susaki, T.; Mamiya, K.; Harada, T. *J. Electron Spectrosc. Relat. Phenom.* **1998**, *88*, 361.
- (61) Zhao, G.; Callaway, J.; Hayashibara, M. *Phys. Rev. B* **1993**, *48*, 15781.
- (62) Miyauchi, H.; Koide, T.; Shidara, T.; Nakajima, N.; Kawabe, H.; Yamaguchi, K.; Fujimori, A.; Fukutani, H.; Iio, K.; Miyadai, T. *J. Electron Spectrosc. Relat. Phenom.* **1996**, *78*, 255.
- (63) Koningsberger, D.; Prins, R. *X-Ray Absorption: Principles, Applications, Techniques of EXAFS, SEXAFS, and XANES*; Wiley Interscience: New York, 1988; Vol. 92.
- (64) Teo, B.; Joy, D. *EXAFS Spectroscopy: Techniques and Applications*; Plenum Press: New York, 1981.
- (65) van Bokhoven, J.; Ressler, T.; de Groot, F. M.; Knop-Gericke, A. *In-Situ Spectroscopy of Catalysts*; American Scientific Publishers: Stevenson Ranch, CA, 2004.
- (66) Castner, D. G.; Watson, P. R.; Chan, I. Y. *J. Phys. Chem.* **1990**, *94*, 819.
- (67) Paul, J.-F.; Payen, E. *J. Phys. Chem. B* **2003**, *107*, 4057.
- (68) Tye, C. T.; Smith, K. J. *Top. Catal.* **2006**, *37*, 129.

- (69) Lauritsen, J.; Nyberg, M.; Nørskov, J. K.; Clausen, B.; Topsøe, H.; Lægsgaard, E.; Besenbacher, F. *J. Catal.* **2004**, *224*, 94.
- (70) Garcia, M. V.; Lindner, J.; Sachdev, A.; Schwank, J. *J. Catal.* **1989**, *119*, 388.
- (71) Bouwens, S.; Van Veen, J.; Koningsberger, D.; De Beer, V.; Prins, R. *J. Phys. Chem.* **1991**, *95*, 123.
- (72) Tan, A.; Harris, S. *Inorg. Chem.* **1998**, *37*, 2215.
- (73) Ho, T. C. *Catal. Lett.* **2003**, *89*, 21.
- (74) Jaramillo, T. F.; Jørgensen, K. P.; Bonde, J.; Nielsen, J. H.; Hørch, S.; Chorkendorff, I. *Science* **2007**, *317*, 100.
- (75) Kibsgaard, J.; Chen, Z.; Reinecke, B. N.; Jaramillo, T. F. *Nat. Mater.* **2012**, *11*, 963.
- (76) Chen, Z.; Cummins, D.; Reinecke, B. N.; Clark, E.; Sunkara, M. K.; Jaramillo, T. F. *Nano Lett.* **2011**, *11*, 4168.
- (77) Kibsgaard, J.; Jaramillo, T. F.; Besenbacher, F. *Nat. Chem.* **2014**, *6*, 248.
- (78) Kong, D.; Wang, H.; Cha, J. J.; Pasta, M.; Koski, K. J.; Yao, J.; Cui, Y. *Nano Lett.* **2013**, *13*, 1341.
- (79) Kong, D.; Cha, J. J.; Wang, H.; Lee, H. R.; Cui, Y. *Energy Environ. Sci.* **2013**, *6*, 3553.
- (80) Cabán-Acevedo, M.; Kaiser, N. S.; English, C. R.; Liang, D.; Thompson, B. J.; Chen, H.-E.; Czech, K. J.; Wright, J. C.; Hamers, R. J.; Jin, S. *J. Am. Chem. Soc.* **2014**, *136*, 17163.
- (81) Faber, M. S.; Lukowski, M. A.; Ding, Q.; Kaiser, N. S.; Jin, S. *J. Phys. Chem. C* **2014**, *118*, 21347.
- (82) Faber, M. S.; Dziedzic, R.; Lukowski, M. A.; Kaiser, N. S.; Ding, Q.; Jin, S. *J. Am. Chem. Soc.* **2014**, *136*, 10053.
- (83) Newville, M. *J. Synchrotron Radiat.* **2001**, *8*, 322.
- (84) Ravel, B.; Newville, M. *J. Synchrotron Radiat.* **2005**, *12*, 537.
- (85) Ravel, B. *J. Synchrotron Radiat.* **2001**, *8*, 314.